Magnetoconductivity of two-dimensional electrons on liquid helium: Experiments in the fluid phase

M. J. Lea, P. Fozooni, A. Kristensen, P. J. Richardson, and K. Djerfi
Department of Physics, Royal Holloway, University of London, Egham, Surrey TW20 0EX, England

M. I. Dykman and C. Fang-Yen
Department of Physics and Astronomy, Michigan State University, East Lansing, Michigan 48824

A. Blackburn
Department of Electronics and Computer Science, University of Southampton, SO17 1BJ, England

The magnetoconductivity $\sigma(B)$ of two-dimensional electrons on liquid helium was measured from 0.25 to 1.3 K in the electron fluid phase in magnetic fields up to 8 T. In low magnetic fields B, $\sigma(0)/\sigma(B) = 1 + (\mu B)^2$ as in the Drude model, where μ is the zero-field mobility due to scattering by ^{4}He vapor atoms and ripplons, even for $\mu B \gg 1$. The values of mobility are in good agreement with previous measurements and with calculations for a correlated electron fluid. At higher fields, $\sigma(0)/\sigma(B)$ deviates from the Drude model and becomes density dependent due to many-electron effects. Only at the highest fields, or the lowest densities, does $\sigma(B)$ approach the theoretical single-particle magnetoconductivity. For both vapor-atom and ripplon scattering the results are in good agreement with a microscopic many-electron theory in which the diffusion of the cyclotron orbits is controlled by the internal fluctuational electric fields. The density and temperature dependence of these internal fields derived from the experiments are in excellent agreement with Monte Carlo simulations. [S0163-1829(97)06024-4]

I. INTRODUCTION

Two-dimensional electrons in surface states above superfluid helium form the simplest conducting system known experimentally.[1] Below 1 K the electrons are in the quantum ground state of the potential well formed by the helium surface and a vertical electric field. However, they are free to move horizontally with very high mobilities μ, limited by scattering from ^{4}He vapor atoms and by the thermal surface vibrations, or ripplons. For vapor atoms the scattering may be regarded as almost ideal, short-range, and quasielastic while ripplon scattering is also well understood. At the electron densities which are stable on bulk helium, $n < 2 \times 10^{13}$ m^{-2}, the electrons in the fluid phase are dilute (typical separation 1 μm), classical, and nondegenerate. However, the electrons are strongly interacting via long-range Coulomb forces, with a macroscopic screening length determined by the distance to underlying metallic electrodes (≈ 100 μm in these experiments.) In most experiments, the plasma parameter (the ratio of the characteristic unscreened Coulomb energy to the kinetic energy), $\Gamma = e^2(\pi n)^{1/2}/4\pi\varepsilon_0 kT \gg 1$, while for $\Gamma > 127$ (low T) the system forms a two-dimensional (2D) electron crystal.[2] Given the experimental flexibility and control over the density, temperature, mobility, and magnetic field, this is an ideal system for investigating the influence of electron-electron interactions on fundamental transport properties.

In particular, recent data clearly indicates that electron-electron interactions, and the internal electric fields which they produce, have a dramatic influence on the magnetoresistivity[3] and magnetoconductivity[4,5] in this system. A single-particle approach will not suffice. Experimentally, the low field magnetoconductivity and magnetoresistivity follow the simple Drude model over a very wide range of conditions, even for $\mu B = \omega_c \tau \lesssim 500$, well in the range of classically strong magnetic fields ($\omega_c = eB/m$ is the cyclotron frequency). This is rather surprising, given that Landau level quantization should occur with energy levels at $(N + 0.5)$ $\hbar\omega_c$ for $\mu B > 1$. The energy density of states will change dramatically with magnetic field and would be expected to enhance the elastic scattering rate, depending on the width of the Landau levels. For independent electrons, the only contribution to this width is the collision broadening, which can be found from the self-consistent Born approximation[6] (SCBA) or from the method of moments[7] which give similar results. This approach works well for low mobility samples,[8] though with some residual quantitative discrepancies, but at higher mobilities ($20 < \mu < 2000$ m^2/V s), the narrower collision width becomes less than the energy spread given by the product of the many-electron internal force $e\mathbf{E}_f$ and characteristic lengths such as the thermal de Broglie wavelength and the quantum magnetic length. This essentially smears out the density of states and leads back to the Drude model for magnetic fields less than some *onset field* B_0, which is typically 0.5 T for electrons on helium. For $B > B_0$, σ_{xx} becomes density dependent and $1/\sigma_{xx}$ is then directly proportional to the internal electric field strength. At higher fields the collision width of the Landau levels increases again and the independent electron theory (SCBA) does become valid. Previous measurements and interpretations of the magnetoconductivity only considered single-particle theories.[9] The many-electron transport effects have been studied theoretically in the extreme quantum limit of strong magnetic field[10] and interesting density-

dependent effects were observed in cyclotron resonance.[11] Recently, the damping of edge magnetoplasmons has been used to determine the magnetoconductivity σ_{xx},[12] both in the vapor-atom and ripplon scattering regimes, in good agreement with the direct measurements reported previously[3,4] and in this paper and confirming the influence of many-electron effects.

Recently a comprehensive many-electron theory of transport phenomena in strongly correlated classical and semi-classical systems has been developed.[13] In parallel with this increased theoretical understanding we have also developed the experimental techniques based on high-precision Corbino electrodes, fabricated using modern lithographic techniques. These new electrodes give improved experimental resolution.

This paper describes measurements of σ_{xx} from 0.25 to 1.3 K in the 2D electron fluid phase, at fields up to 8 T, in both the vapor-atom and ripplon scattering regimes. The paper is organized as follows. In Sec. II we give an account of the basic theoretical concepts underlying many-electron magnetoconductivity within the framework of the Einstein diffusion relation. In Sec. III we describe the experimental cell, the Corbino electrodes, and the experimental procedures. In Sec. IV we give the experimental results and analyze them in terms of the internal electric fields in the 2D system while in Sec. V we draw the main conclusions and the Appendix gives some of the theoretical expressions used.

II. MAGNETOCONDUCTIVITY

A. Zero-field mobility

The zero-field mobility μ and the zero-field conductivity $\sigma_0 = ne\mu$ in the 2D electron fluid have been measured by many authors using rectangular electrodes (the original Sommer-Tanner technique[14]), circular Corbino electrodes,[15,16] the plasma linewidth,[17] or a resonant cavity at radio frequencies.[18] The most detailed measurements in zero field are those of Mehrotra et al.[19] below 1 K, using frequencies up to 2 MHz and by Stan and Dahm.[20] The mobility is strongly temperature dependent and varies from 1 m²/V s just below the λ point to over 2000 m²/V s at 0.1 K (depending on the density). Within the single-particle approximation, the zero-field mobility has been calculated for vapor-atom and ripplon scattering by Saitoh,[21] using the electron-ripplon interaction[22] which depends strongly on the perpendicular electric pressing field $E_\perp$. However, Buntar' et al.[18] pointed out that the electron-electron correlation time for $n \geqslant 10^{12}$ m^{-2} is less than the electron-ripplon relaxation time. For an energy dependent interaction (such as with ripplons, but not vapor atoms) this leads to a different average in the expression for μ which can be a factor of 2 smaller than the single-particle result (in Ref. 18 the effect was considered in terms of occasional electron-electron collisions as if the electron system were a weakly nonideal plasma). For a strongly correlated classical electron system the zero magnetic field scattering rate τ_0^{-1} is shown in the Appendix to be of the form

$$\tau_0^{-1} = \frac{e^2 E_\perp^2}{4\hbar\alpha_s}\left[1 + \frac{E_1}{E_\perp} + \frac{E_2^2}{E_\perp^2}\right], \tag{1}$$

where α_s is the surface tension and E_1 and E_2 are explicit integrals which are functions of the temperature T and the vertical pressing field $E_\perp$ as given in the Appendix. This expression is valid for $\hbar\omega_p/kT \ll 1$ where $\omega_p = (e^2 n^{3/2}/2\varepsilon_0 m)^{1/2}$ is the characteristic frequency of short-wavelength 2D plasmons. However, the numerical values for the mobility given by Eq. (1) are very close to those from Saitoh's expressions[21] and also the calculations done by Mehrotra et al.[19] For higher densities the motion of an electron in the field of other electrons is no longer classical. The analysis of this case is beyond the scope of the present paper.

B. Conductivity as diffusion: The Einstein relation

The Drude model gives the magnetoconductivity of a 2D electron system (2DES) by assuming independent electrons in classical orbits in a magnetic field and a field-independent scattering time. The tensor components of the magnetoconductivity σ and magnetoresistivity ρ are as follows (the signs of the components given are positive for negative charges, putting $e = |e|$):

$$\sigma_{xx} = \frac{\sigma_0}{(1 + \mu^2 B^2)}, \quad \sigma_{yx} = \mu B \sigma_{xx}, \tag{2a}$$

$$\rho_{xx} = \rho_0, \quad \rho_{xy} = B/ne. \tag{2b}$$

These simple results act as benchmarks for our experiments to measure σ_{xx}. A useful parameter to plot experimentally is the ratio $ne/\mu\sigma$ which for the Drude model at $\mu B \gg 1$ becomes

$$\frac{ne}{\mu\sigma(B)} \approx B^2. \tag{3}$$

Conductivity in a 2D electron fluid is essentially a diffusion process. The Einstein relation between mobility and the diffusion constant for a system obeying Maxwell-Boltzmann statistics gives

$$\sigma_{xx} = \frac{ne^2}{kT}\frac{L^2}{\tau_B}, \tag{4}$$

where L is the diffusion length and τ_B^{-1} is the scattering rate in a field. In zero magnetic field, putting $2L^2$ equal to the squared mean free path reproduces $\sigma_0 = ne\mu$. In a magnetic field the diffusion length is given by $L^2 = R_c^2/2$, where $R_c = (2mkT)^{1/2}/eB$ is the classical cyclotron radius, for $\hbar\omega_c/kT \ll 1$, while for $\hbar\omega_c/kT \gg 1$, only the lowest Landau level is occupied and $L^2 = l^2/2$ where $l = (\hbar/eB)^{1/2}$ is the magnetic length. The various conductivity models correspond to selecting the value of L and the scattering rate,[23] as shown in Table I. The Einstein model is, of course, equivalent to the orbit-center migration theory of Kubo et al.[24] and Ando et al.[6]

The Drude model, for $\mu B \gg 1$, is given by classical cyclotron orbits and $\tau_B = \tau_0$, which leads to $ne/\mu\sigma = B^2$ as shown in Table I. But the Drude model neglects the quantization of electron orbits into Landau levels, which changes the scattering rate via the density of states. In the self-consistent Born approximation (SCBA) for δ-function scatterers, as discussed by Ando et al.[6] for degenerate electrons, the Landau

TABLE I. 2D magnetoconductivity for short-range scattering, using the Einstein relation, for $\omega_c\tau_B\gg1$. $\sigma=(ne^2/kT)(L^2/\tau_B)$; $R_c=(2mkT)^{1/2}/eB$; $l=(\hbar/eB)^{1/2}$.

Model	L^2	$\dfrac{\tau_0}{\tau_B}$	$\dfrac{ne}{\mu\sigma}$
Drude-classical	R_c^2	$=1$	$=B^2$
Drude-quantum	l^2	$=1$	$\propto BT$
Single electron Landau levels Classical orbits	R_c^2	$\propto(\mu B)^{1/2}$	$\propto\dfrac{B^{3/2}}{\mu^{1/2}}$
Single electron Landau levels Quantum orbits	l^2	$\propto(\mu B)^{1/2}$	$\propto\dfrac{TB^{1/2}}{\mu^{1/2}}$
Many-electron Landau levels Classical orbits $B\gg B_0$	R_c^2	$\propto\hbar\omega_c/\Delta_c$ $[\Delta_c=eE_fR_c]$	$=\pi B_0^2$ $B_0^4=\dfrac{2m^3kT\langle E_f^2\rangle}{\hbar^2 e^2}$
Many-electron Landau levels Quantum orbits	l^2	$\propto\hbar\omega_c/\Delta_q$ $[\Delta_q=eE_f l]$	$=\dfrac{4B_0^2}{(\hbar\omega_c/kT)^{1/2}}$

levels are collision broadened to a width $\Delta_s=\hbar/\tau_B$. Hence the scattering rate is enhanced by a factor $\sim\hbar\omega_c/\Delta_s$ as the electron states from an energy range $\hbar\omega_c$ are concentrated into Δ_s. For a semielliptical density of states[6] at each Landau level this leads to the self-consistent result $1/\tau_B=(2\mu B/\pi)^{1/2}/\tau_0$. An expression for the resultant magnetoconductivity for a nondegenerate 2D electron gas has been given by van der Heijden *et al.*[25] The functional dependences of $ne/\mu\sigma$ are given by the Einstein relation as shown in Table I. Scheuzger *et al.*[26] derived the corresponding expressions for Gaussian density of states, with slightly different prefactors (the factor $2/\pi$ becomes $1/2$). The original SCBA theory was only valid for $\sigma_{xx}/\sigma_{yx}\gg1$ but it has been extended to all values of this ratio,[27] keeping $\omega_c\tau_B\gg1$, and gave an excellent fit to data on edge-mode propagation for electrons on helium at temperatures above 1.7 K at very high magnetic fields (up to 22 T), where the vapor-atom scattering is very strong.[25] It is our contention that as the mobility increases, electron-electron interactions become increasingly important.

The corresponding SCBA theory for the magnetoconductivity for ripplon scattering in the 2D electron fluid has been given by Saitoh[28] for $\hbar\omega_c/kT>1$, who also calculated $\sigma_{xx}(B)$ for the 2D solid phase.

C. Many-electron effects

In the relatively dilute 2DES on helium, there is negligible wave function overlap and the force on an individual electron can be expressed in terms of a local fluctuating electric field $\mathbf{E}_f$. The distribution of $\mathbf{E}_f$ for a classical normal liquid has been obtained in several ways. Since fluctuations in the system are thermal, and the field arises because of the electron-electron interactions, it is convenient to write the mean-square field in the form

$$\langle E_f^2\rangle=F(\Gamma)\left(\frac{2mkT\omega_p^2}{e^2}\right)=F(\Gamma)\left(\frac{kTn^{3/2}}{4\pi\bar{\varepsilon}\varepsilon_0}\right)=F(\Gamma)E_0^2,$$
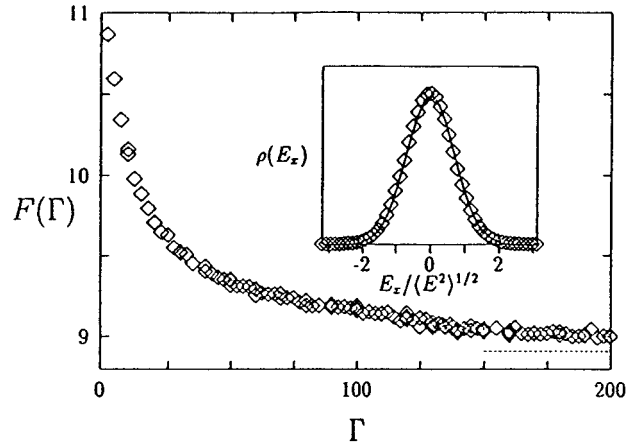(5)

FIG. 1. The scaled mean square field $F(\Gamma)$ from Monte Carlo calculations. The asymptotic value of $F=8.91$ for a harmonic classical Wigner crystal is shown dashed. Inset: the field component distribution.

where $\omega_p=(e^2n^{3/2}/2\varepsilon_0 m)^{1/2}$ is the 2D plasma frequency with a wave vector $q=n^{1/2}$ and $\bar{\varepsilon}=1.0286$. The force driving an electron can be calculated for large Γ (low T) in the 2D crystal phase[29] and arises because of the displacement of the electrons from the lattice sites $\mathbf{R}_i$. In the harmonic approximation it is linear in the displacement, has a Gaussian distribution, and $F(\Gamma)=8.91$, independent of Γ. In the most interesting range of the normal electron liquid and of the melting transition the function $F(\Gamma)$ has been obtained from Monte Carlo simulations in Ref. 30 and is plotted in Fig. 1. The variation of F is surprisingly small in this range, varying from 9.1 at $\Gamma=200$ to 9.5 for $\Gamma=20$ although the structure of the system changes dramatically from a good crystal to a liquid whose correlations decay over a few electron spacings. Previous analyses and calculations of the many-electron magnetoconductivity in the fluid phase invoked short-range order[31] and used the value $F=8.91$.

The effects of these internal fields on the magnetotransport can be considered in several ways. The basic ideas can be simply understood in terms of cyclotron orbit diffusion. The scattering rate for elastic scattering depends on the electron density of states or smearing of the Landau levels. In the single-particle SCBA this smearing is the Landau level collision width $\Delta_s=\hbar/\tau$. But for a fluctuating many-electron field of magnitude E_f, there are other characteristic energies. For $\hbar\omega_c/kT\ll1$, the characteristic ''size'' of the electron is the thermal de Broglie wavelength $\lambdabar_T=\hbar/\sqrt{2mkT}$. Hence there is a quantum uncertainty of the kinetic energy of the electron wave packet $\Delta_K=\lambdabar_T eE_f$ due to the fluctuating internal fields. For $\Delta_K>\hbar\omega_c$, which corresponds to $\omega_p>\omega_c$, or $B<0.23$ T for $n=10^{12}$ m^{-2}, Landau level quantization is smeared out and the orbit diffusion and magnetoconductivity are essentially the same as in the Drude formalism. This is also the case for $\Delta_c=eE_fR_c>\hbar\omega_c$, where Δ_c is the energy variation across a cyclotron orbit radius R_c. The condition $\Delta_c=\hbar\omega_c$ defines a characteristic magnetic field $B_0=9.69\times10^{-6}F^{1/4}n^{3/8}T^{1/2}$ T which is the onset field for magnetoresistance and for deviations from Drude-like magnetoconductivity, and lies between 0.2 and 1 T in these experi-

ments. Only for $\Delta_c \lesssim \hbar \omega_c$ do the Landau levels influence the magnetoconductivity as the smearing of the Landau levels becomes less than the level separation.[3] For $B > B_0$, the scattering rate is then enhanced by a factor $\tau_B^{-1}/\tau_0^{-1} \approx \hbar \omega_c/\Delta_c$, as shown in Table I, and we obtain the striking result

$$\frac{ne}{\mu\sigma(B)} = \frac{\tau_B^{-1}}{\tau_0^{-1}} B^2 = \pi B_0^2 = 8.50 \times 10^{-4} E_f \sqrt{T}, \quad \hbar\omega_c/kT \ll 1, \tag{6}$$

which may be compared with Eq. (3). In this region, $ne/\mu\sigma(B)$ is directly proportional to the rms internal electric field $E_f = \langle \mathbf{E}_f^2 \rangle^{1/2}$ (this result is strictly valid only for short-range scatterers).

In the quantum limit, $\hbar\omega_c/kT > 1$, the characteristic length scale is the magnetic length l. This affects the magnetoconductivity σ in two ways. First the diffusion length changes and this in itself would give magnetoresistance and deviations from the classical Drude model, even for field-independent scattering, as in the quantum Drude model in Table I. Also the energy spread across the cyclotron orbit is $\Delta_q = eEl$. Hence, for $\Delta_q < \hbar\omega_c$, we obtain (for short-range scatterers)

$$\frac{ne}{\mu\sigma(B)} = \frac{4B_0^2}{(\hbar\omega_c/kT)^{1/2}}, \quad \hbar\omega_c/kT \gg 1. \tag{7}$$

Note that $ne/\mu\sigma$ is still proportional to the internal electric field strength E_f.

In all cases the scattering rate increases with field and at the highest fields, the Landau level collision width Δ_s can become greater than Δ_q and the SCBA result for quantum orbit diffusion should then apply, as shown in Table I. It is also interesting to note that the scattering rate increases with magnetic field faster than the cyclotron frequency and hence the Hall angle $= \tan^{-1}(\sigma_{xx}/\sigma_{yx}) = \tan^{-1}(\mu B)$ in low fields, decreases as B increases.[25] The Hall effect has been measured in this system and there is strong experimental and theoretical evidence that a linear Hall effect, $\rho_{xy} = B/ne$ is always valid in a nondegenerate 2D electron fluid.

The internal field that drives an electron during its collision with a scatterer fully characterizes the effect of the electron-electron interaction on electron scattering provided the field is uniform over the electron wavelength and does not change during a collision. These conditions are met if the electron motion is classical or semiclassical. For $B = 0$ this requires that the change of the electron energy over a thermal wavelength $\lambdabar_T$ be small compared to the thermal energy, or $eE\lambdabar_T \ll kT$.[32] This corresponds to the condition $\hbar\omega_p \ll kT$. In this limit, the scattering rate (for short-range scatterers) is only slightly enhanced by a factor $1 + (5F/384\pi)(\hbar\omega_p/kT)^2 \approx 1 + 0.04(\hbar\omega_p/kT)^2$ for $\omega_p\tau \gg 1$.[13] However, the condition $\hbar\omega_p/kT = 3.4 \times 10^8 n^{3/4}/T > 1$ can be easily reached and this may account for some of the density dependent scattering seen by Mehrotra *et al.*[19] for $n > 2 \times 10^{12}$ m^{-2}.

Hence we see that the conductivity of a nondegenerate 2D electron gas depends on the relative magnitudes of four relevant energy scales: the thermal energy kT, the characteristic plasmon energy $\hbar\omega_p = \Delta_K$, the cyclotron energy $\hbar\omega_c$,

and the energy variations $eE_f l \tanh(\hbar\omega_c/2kT)$ across the electron wavelength. The next two sections give more detailed equations used in the analysis.

D. Vapor-atom scattering

The dominant scattering above 1 K comes from the ^{4}He vapor atoms which act as almost ideal short-range scattering centers. Because of the large mass ratio such scattering is quasielastic. In the whole range of classical magnetic fields $\hbar\omega_c/kT \ll 1$, the normalized many-electron classical magnetoresistance ρ_{mc}^* and magnetoconductivity σ_{mc}^* can be written in the form[13]

$$\rho_{mc}^* = \frac{\rho_{xx}}{\rho_0} = \mu^2 B^2 \sigma_{mc}^* = \frac{\tau_B^{-1}}{\tau_0^{-1}}$$

$$= \sum_{s=-\infty}^{\infty} (1 + 4\pi^2 s^2 (B_0/B)^4)^{-3/2}, \quad \hbar\omega_c/kT \ll 1, \tag{8a}$$

$$B_0 = \left[\frac{2m^3 kT \langle E_f^2 \rangle}{\hbar^2 e^2} \right]^{1/4},$$

$$\frac{ne}{\mu\sigma(B)} = \frac{\tau_B^{-1}}{\tau_0^{-1}} B^2 = \frac{B^2}{\rho^*}, \quad \text{for } \omega_c\tau \gg 1. \tag{8b}$$

The normalized magnetoresistance is a function of the onset field B_0. For $B \ll B_0$ there is zero magnetoresistance, and the magnetoresistivity and magnetoconductivity follows the Drude model. Deviations from the Drude model start for $B \approx B_0$ with a limiting value given by Eq. (6).

For $(B^3 kT m/eB_0^4) \tanh(\hbar\omega_c/kT) \gg 1$ and for arbitrary $\hbar\omega_c/kT$ the normalized many-electron quantum magnetoresistance is

$$\rho_{mq}^* = \frac{B^2}{4B_0^2} \left(\frac{\hbar\omega_c}{kT} \right)^{1/2} \Xi, \tag{9a}$$

$$\frac{ne}{\mu\sigma(B)} = \frac{4B_0^2}{\Xi \sqrt{\hbar\omega_c/kT}}, \tag{9b}$$

where the factor Ξ allows for the filling of the Landau levels and is a function of $\hbar\omega_c/kT$; $\Xi = 1$ in the quantum limit. Equations (8) and (9) agree exactly for $B \gg B_0$ and $\hbar\omega_c/kT \ll 1$.

In the vapor-atom scattering regime above 1 K, the Landau level collision width Δ_s is comparable with the energy spread due to the internal electric fields, particularly above 3 T. The Einstein relation gives $\sigma \propto \tau_B^{-1}$ in strong B. If the cyclotron orbits have a spread of energies Δ then the scattering rate is enhanced, due to the concentration of the density of states, by a factor proportioned to $\hbar\omega_c/\Delta$. If we write $\Delta^2 = (\hbar\tau_B^{-1})^2 + \Delta_m^2$ as the sum of collision broadening and many-electron effects then

$$\frac{1}{\tau_B} \approx \frac{1}{\tau_0} \frac{\hbar\omega_c}{\sqrt{\Delta_m^2 + (\hbar/\tau_B)^2}}. \tag{10}$$

For $\Delta_m = 0$, this gives the SCBA result $\sigma_s \propto \sqrt{\omega_c \tau_0}$, while for many-electron fields only, $\sigma_m \propto (\hbar \omega_c / \Delta_m)$. In combination, the total conductivity σ is approximately given by

$$\frac{1}{\sigma^2} = \frac{1}{\sigma_m^2} + \frac{\sigma^2}{\sigma_s^4}. \qquad (11)$$

An alternative combination[4] could also be used.

E. Ripplon scattering

The magnetoconductivity due to ripplon scattering differs from the vapor-atom scattering case in that we must allow for the finite correlation length of the random potential of the ripplons. In zero field and for $\hbar \omega_c / kT \ll 1$ the dominant scattering comes from ripplons whose wavelength is of the order of (or greater than) the thermal de Broglie wavelength, and hence independent of B and electron density. At 1 K these ripplons have a wavelength ≥ 0.13 μm, a frequency ≤ 80 MHz, and an energy $\leq 0.004 kT$. Thus the magnetoconductivity behaves in a similar way to short-range scattering, Eqs. (2), (6), and (8). For $\hbar \omega_c / kT \ll 1$ and for $B < B_0$, the ''Drude'' model is followed, Eq. (2), with a scattering rate and mobility given by Eq. (1). For $B > B_0$, $ne/\mu\sigma$ approaches an almost field-independent limit as σ saturates. Explicit expressions for σ in the ripplon scattering regime are given in the Appendix and a fuller account in Ref. 13.

In the range $B \geq B_0$ the results for ripplon scattering are somewhat different from the results for short-range scattering. But the function $\sigma^{-1}(B)$ still has a maximum. The ripplon magnetoconductivity has been analyzed in Ref. 13. In the range of quantizing fields

$$\frac{ne}{\mu\sigma(B)} = \frac{4B_0^2}{(\hbar\omega_c/kT)^{1/2}} G(T,B,E_\perp), \quad \hbar\omega_c/kT \gg 1, \qquad (12)$$

where the factor $G(T,B,E_\perp)$ allows for the field-dependent interaction from the changing wave vector $\mathbf{q}$ of the scattering ripplons. It is rather remarkable that this factor is relatively close to unity for a wide range of densities and fields. The mobility used in Eq. (12) is the zero-field mobility, allowing for many-electron effects and should be the mobility as measured from the Drude relation, Eq. (2). The parameter $ne/\mu\sigma$ is again proportional to the internal electric field strength E_f.

In the region from 0.8 to 1.1 K both ripplon and vapor-atom scattering are significant. From Eq. (2) the total conductivity is just the sum of the two separate contributions, $\sigma = \sigma_1 + \sigma_2$. Allowing for the self-consistent combination of many-electron and collision effects, as in Eq. (10), the contributions σ_1 and σ_2 can be estimated by solving two simultaneous equations, where σ_{mi} is the conductivity from the ith scattering mechanism ($i = 1, 2$) due to many-electron effects alone, while σ_{si} is the conductivity from the independent electron theory,

$$\frac{1}{\sigma_i^2} = \frac{1}{\sigma_{mi}^2} + \frac{\sigma^2}{\sigma_{si}^4}. \qquad (13)$$

Note that for many-electron effects alone this gives $\sigma = \sigma_{m1} + \sigma_{m2}$, while for the SCBA single-particle approximation with no many-electron fields, $\sigma^2 = \sigma_{s1}^2 + \sigma_{s2}^2$.
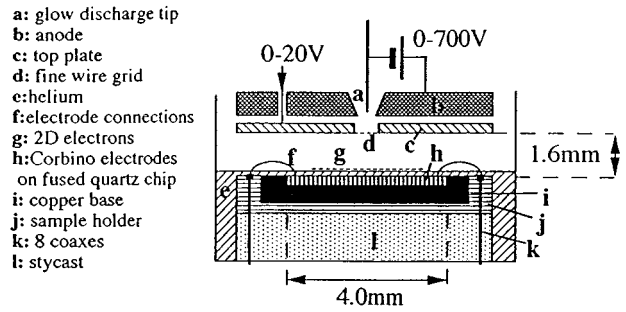

a: glow discharge tip
b: anode
c: top plate
d: fine wire grid
e: helium
f: electrode connections
g: 2D electrons
h: Corbino electrodes on fused quartz chip
i: copper base
j: sample holder
k: 8 coaxes
l: stycast

FIG. 2. Schematic diagram of the experimental cell.

III. EXPERIMENTAL PROCEDURES

A. Experimental cell

The experimental cell is shown in Fig. 2. It is made of OFHC copper and mounted on a dilution refrigerator inside a 9 T superconducting magnet. The measurement electrodes **h** (see next section) are mounted in a copper base-plate **i** about 100 μm below the surface of the superfluid helium **h**. Electrical leads **f** are taken into the cell using stycast lead-throughs. All the leads to the electrodes were through 50 Ω coaxial cables **k** to reduce the interlead capacitance. A top-plate **c** is situated 1.6 mm above the electrodes. Free electrons are generated using a glow discharge from a 50 μm tungsten wire **a** at about -400 V. This operates between 1.25 and 1.6 K when the helium vapor pressure lies between 1 and 7 mbar. A typical discharge current is 50 nA. The electrons are thermalized and pass through a 100 μm mesh grid **d**, set in the top plate, into the experimental space. The electrons are controlled by dc potentials on the electrodes, the top plate and the base plate. The maximum, or saturated, electron density occurs when the potential on the electron sheet equals the top-plate voltage V_T and is given by $n_s = \varepsilon\varepsilon_0 V_T / ed$. In practice, the magnitude of the top-plate potential was usually increased after charging so that n was below the saturation density.

Ultrapure [4]He (Ref. 33) was used to fill the cell. The [3]He content was exceptionally low. This was to avoid any effects due to the formation of a [3]He-rich surface layer at low temperatures, which might alter the mobility as found experimentally by Esel'son *et al.*[34]

B. The Corbino-disk electrodes

The conductivity of the 2DES on liquid helium was measured using the circular Corbino disk geometry. To obtain precisely defined electrode structures, we used optical lithography and the device fabrication techniques of the Southampton University Microelectronics Centre.[35] The geometry of the Corbino disk, with 6 coplanar electrodes on polished fused quartz, is shown in Fig. 3. A central (or drive) electrode A was surrounded by a ring electrode E which also separated the annular receiving electrode B into three segments $B1$, $B2$, and $B3$. Round these was a planar guard electrode G. Two metallic gold layers were deposited, insulated by an intervening SiO$_2$ layer. The electrodes were all in the upper metal layer. Electrical contact to the inner electrodes was made along strips in the lower metal layer which ran under the guard G and electrode E. These made contact
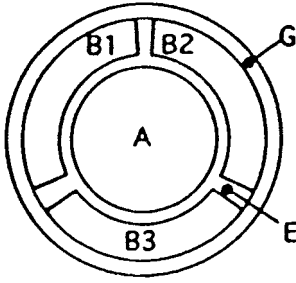
FIG. 3. The geometry of the Corbino electrodes.

to the upper metal electrodes through vias etched in the SiO$_2$ dielectric layer. Finally, 25 μm gold wires were bonded to pads on the outside of the 5×5 mm^2 polished quartz chip, leading to coaxial cables.

The electrons were held in place by dc potentials on electrodes A, B, and E (dc ground), the guard electrode G ($-ve$) and the top plate ($-ve$). The diameter of the electron sheet was 4 mm. The gap between neighboring electrodes was only 10 μm and so we were able to set the depth d of the helium above the electrodes to be as low as 50 μm (an order of magnitude lower than any previous Corbino experiment) while maintaining a uniform electron density across the gaps. This gave several significant advantages (though some disadvantages). The segmented electrode structure enabled the helium surface to be leveled to better than 1 μm. A large ac voltage (0.1 V) was applied to electrode A and the ac currents to the three segments of electrode B were measured independently as the cryostat was tilted. These currents could be balanced to better than 1% by leveling the cryostat using three air mounts (corresponding to 1 mrad). The tilt of the cryostat was subsequently monitored using three displacement sensors.

The fractional change in these three signals, on tilting by a measured amount, also enabled the depth of the helium to be determined, since each current is inversely proportional to the depth of helium over the electrode. The electron density profile was calculated numerically, for a given set of electrode potentials, by the method of relaxation, from Poisson's equation.[36] For $d=50$ μm the electron density was very uniform and the width of the edge layer was only 3% of the radius. The height decreased, as the temperature dropped, by about 15 μm between 1.3 and 0.3 K, below which it was almost constant. The origin of this effect is not clear, though it may be due to the increasing surface tension of the helium[37] which pulls more liquid up the walls and hence decreases the bulk level. The height was also slightly magnetic-field dependent, $\Delta d \approx B^2$, presumably due to residual inhomogeneities in the field profile of the magnet across the helium surface.[38]

The vertical electric field $E_\perp$ has been discussed by Yücel et al.[39] However, we use a slightly different expression for our experiments. For a top plate at a voltage V_T a distance D above grounded electrodes the field is

$$E_\perp = \frac{-V_T}{a+d/\varepsilon} - \frac{ne}{2\varepsilon_0} \frac{2}{(\varepsilon+1)} \frac{(a-d)}{(a+d/\varepsilon)}, \quad (14)$$

where $a=D-d$. The first term is the applied field while the second term comes from the image charges in the upper and
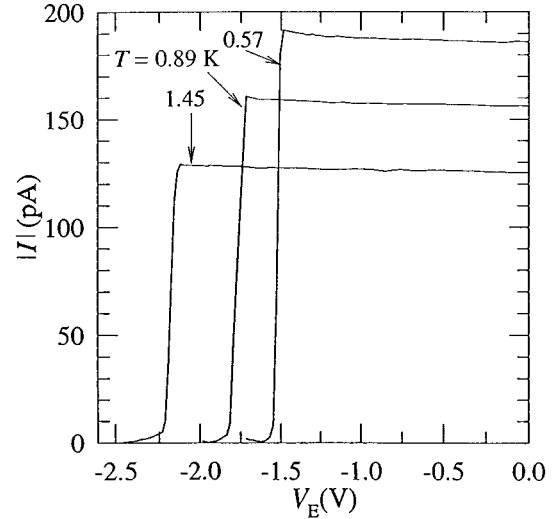

FIG. 4. The cutoff of the electron current as the voltage V_E is varied for the same density at 1.45, 0.89, and 0.57 K. The sharp decrease in current defines the cutoff voltage V_c.

lower metal electrodes. Note that this is the mean electric field seen by an electron in the equilibrium ground state for motion perpendicular to the surface and does not include the field from the localised polarization charge associated with each electron. This field contributes to the changes in the electron energy from vertical displacement due to the ripplons and hence to the electron-ripplon interaction. At these low helium heights it is also necessary to consider the pressure on the helium surface due to the vertical electric holding field $E_\perp$. The total pressure p is reduced because of the polarization charge and is given by $P=\varepsilon_0(E_v^2-E_1^2)/2$ where E_v is the vertical electric field in the helium vapor above the electrons and E_1 is the field in the liquid. An electron density $n=1\times10^{12}$ m^{-2} at saturation ($E_v=0$) would produce a depression of the helium surface of 0.9 μm, which is small compared with the typical helium depth of 100 μm, though this depression might become significant at higher densities.

This electrode geometry design also enabled the electron density to be accurately determined (crucial for these experiments) by increasing a $-ve$ dc bias voltage, V_E, on electrode E until the ac current between electrodes A and B cut off sharply, as shown in Fig. 4. An analysis of the electric fields in the cell shows that, for $d<W=200$ μm, the width of the E electrode, the cutoff voltage V_c is independent of the top-plate voltage. The electron density is given by $n=\kappa\varepsilon\varepsilon_0 V_c/ed$, where $\kappa\approx0.84$ is a factor which allows for the electrons displaced from above electrode E. The data sets in Fig. 4 show the cutoff of the capacitative current for the same electron density at 1.45, 0.89, and 0.57 K. It can be seen that the cutoff voltage decreases as the temperature drops while the capacitive current increases, both corresponding to a decrease in the helium height.

The high degree of circular symmetry in these precision electrodes meant that low frequency edge magnetoplasmons[40] (EMP) were not generated.

C. Measurement of magnetoconductivity

An ac voltage V_d between 1 and 200 mV rms (typically 10 mV) at a frequency $f(=\omega/2\pi)$ between 2 and 70 kHz
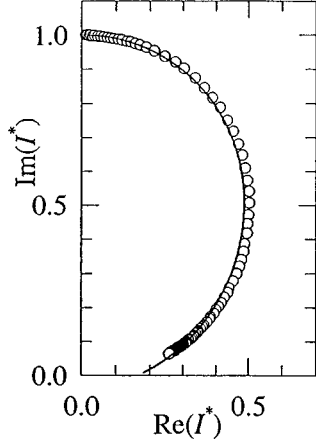
FIG. 5. The normalized resistive component, Re(I^*), vs the capacitive component Im(I^*), of the ac current for the Corbino electrodes used. The solid line shows the theory, Eq. (15); the circles are data taken at 1.3 K for $n = 0.64 \times 10^{12}$ m^{-2} at 70 kHz as the magnetic field increases to 7 T.

was applied to electrode A and the ac current I to the electrodes B was measured using a lock-in amplifier. Electrode E was kept at ac ground. For a perfectly conducting electron sheet the phase of the capacitively coupled current I is $\pi/2$ with respect to V_d. The phase shift $\phi(B)$ away from $\pi/2$ was measured as a function of $B \leqslant 8$ T for a range of electron densities, for temperatures $0.25 \leqslant T \leqslant 1.3$ K. The drive voltage induces a heavily damped voltage wave which propagates on the 2D transmission line formed by the electrons and the underlying electrodes, with a propagation constant k_e. The radius of the inner electrode A is $r_1 = 1.2$ mm. The outer and inner radii of the B electrodes are $r_2 = 2$ mm and $r_3 = 1.4$ mm, respectively. The current which flows to electrode B when electrode A is driven is given by[41]

$$I = i\omega\beta\pi^2 r_1 r_3 C_s \gamma V_d \frac{J_1(k_e r_1)}{J_1(k_e r_2)}$$
$$\times [J_1(k_e r_3) Y_1(k_e r_2) - J_1(k_e r_2) Y_1(k_e r_3)], \quad (15)$$

where J_1 and Y_1 are first-order complex Bessel and Neuman functions, $\gamma = [1 + d/\varepsilon a]^{-1}$, and β is the fraction of the Corbino disk occupied by the B electrodes for $r > r_3$. In the fully screened or local limit and for $\omega\tau \ll 1$ the wave vector $k_e = (1-i)/\delta$, where $\delta = \sqrt{2\sigma_{xx}/\omega C_s}$ and $C_s = \varepsilon_0(1/a + \varepsilon/d)$ is the capacitance per unit area between the electrons and the electrodes.[42] For a given Corbino geometry the measured phase shift is then a function only of the decay length δ, which governs how the phase shift scales with density, frequency, and conductivity. Allowance for incomplete screening and for finite $\omega\tau$ can be made by modifying the propagation vector k_e. For $\delta \gg r_3$, the purely capacitive current is determined by the geometrical capacitance and given by $I_0 = i\omega\beta C_s \gamma V_d \pi r_1^2 (r_2^2 - r_1^2)/r_2^2$. The normalized current $I^* = I/|I_0|$ is plotted on an Argand diagram in Fig. 5 as δ is varied. This plot gives a universal locus and is very useful in validating the data obtained. At the relatively low frequencies used here, the phase shift in zero magnetic field is very small and the measured current below 1 K defines I_0. As
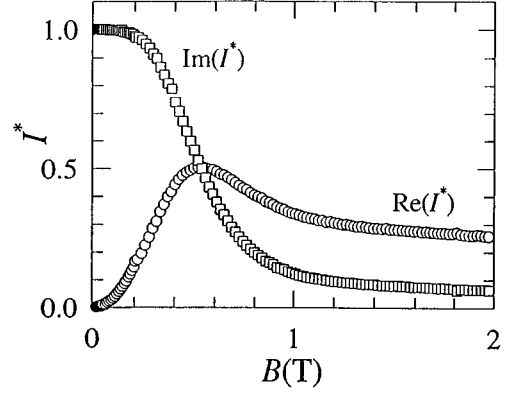

FIG. 6. The normalized resistive, Re(I^*), and capacitive, Im(I^*), components of the ac current as a function of the magnetic field at 1.3 K for $n = 0.64 \times 10^{12}$ m^{-2} at a frequency of 70 kHz.

B increases, the magnetoconductivity decreases and the amplitude and phase of the measured I are field dependent as shown in Fig. 6, where both the capacitative and resistive components of the current are plotted. The same data is plotted on the Argand diagram in Fig. 5, and lies very close to the theoretical response curve. Deviations from the theory on this plot may result from an inhomogeneous electron sheet, which gives rise to edge magnetoplasmons or from finite values of $\omega\tau$. In all the experiments reported here, only data which lay on the line of the theoretical response function was used. The following empirical expression gives an excellent fit to Eq. (15) for calculating the decay length, and hence the magnetoconductivity from values of the phase shift $\phi(B)$ < 1.3 rad,

$$\frac{1}{\delta^2} = \frac{\omega C_s}{2\sigma_{xx}(B)} = \frac{1.92 \times 10^6 \phi(B)}{1 - 0.395\phi^2(B)}, \quad (16)$$

where the constants in the last expression depend on the dimensions of the electrodes and were adjusted to allow for the effect of the guard potential in reducing the size of the electron sheet. For small phase shifts, $\phi < 0.3$, the phase shift is directly proportional to $1/\sigma_{xx}$.

All the measurements reported here are in the linear or Ohmic region. A small quadratic increase in $1/\sigma$ was observed as the drive voltage V_d was increased in the fluid phase. Saitoh[21] has shown that such an increase can be due to a rise in the electron temperature as heat is transferred to the ripplons. For the 10 mV drive normally used, the effect is very small in the fluid phase, though strong nonlinear effects occur in the solid phase.[43]

IV. EXPERIMENTAL RESULTS AND DISCUSSION

A. The Drude region

The magnetoconductivity was measured at temperatures below 1.3 K down to the phase transition to the solid phase at $T_m = 0.225 \times 10^{-6} n^{1/2}$ K (Ref. 44) for densities from 0.5 ($T_m = 0.15$ K) to 4.0 ($T_m = 0.43$ K) $\times 10^{12}$ m^{-2} in magnetic fields up to 8 T. Figure 7 shows $1/\sigma(B)$ versus B at 1.3 K on a log-log plot, measured at the relatively high frequency of 70 kHz to obtain the phase shift in small fields. At
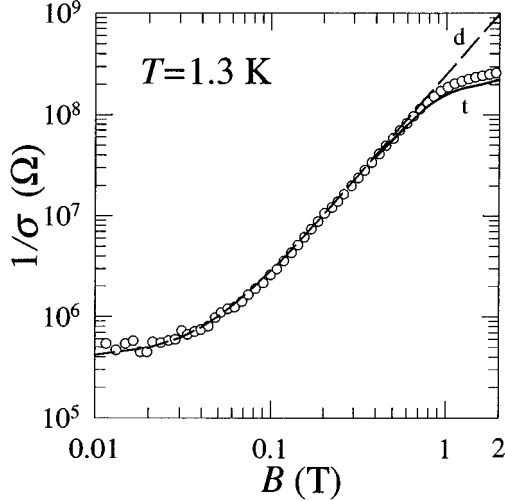
FIG. 7. The Drude region for magnetoconductivity, showing $1/\sigma(B)$ vs B at 1.3 K for $n = 0.64 \times 10^{12}$ m^{-2}. Line **d** shows the fit to the Drude model while line **f** is the full theory including many-electron and single-particle scattering effects.

FIG. 8. The Drude mobility μ vs electron density at 0.6, 0.7, 0.8, and 0.9 K. The solid lines show the theoretical zero-field mobility.

very low fields ($B < 0.02$ T) the reciprocal conductivity $1/\sigma$ is constant but, as $\mu B \gg 1$, increases rapidly and follows a B^2 dependence for over two decades. Line **d** shows the excellent fit to the Drude model, Eq. (2a), with $\mu = 24$ m^2/V s. The phase shift in zero magnetic field could only be measured for these relatively low mobilities. Below 1 K, we find $1/\sigma_{xx} \propto B^2$ at low fields at all temperatures, down to the smallest phase shifts we can resolve at the frequencies used. Following the discussion given above, this Drude behavior implies that the scattering rate is independent of field and hence we can derive experimental values for the electron mobility using Eq. (2a). This method was originally used in this system by Iye[16] and more recently for ^{3}He and ^{4}He.[43,45] Above 1.1 K the scattering is primarily due to gas-atom scattering and the experimental mobility values are generally within 10% of the theoretical values from the expression given by Saitoh.[21] Figure 8 shows a plot of the mobility versus electron density at temperatures of 0.9, 0.8, 0.7, and 0.6 K. The mobility decreases with increasing density because of the increase in the vertical electric holding field $E_\perp$, Eq. (14). These values are in close agreement with the zero-field measurements of Mehrotra *et al.*[19] This agreement confirms the premise that small magnetic fields do not affect the scattering rate. The solid lines show the theoretical expression for the zero-field mobility including gas-atom scattering and ripplon scattering, Eq. (1), as discussed above. For $n = 1 \times 10^{12}$ m^{-2} the fraction of the total scattering rate due to ripplons increases from 0.31 at 0.9 K to 0.97 at 0.6 K. Below 0.6 K, the scattering due to gas atoms is negligible. The electron mobilities below 0.5 K are extremely high. For instance, the data at 0.4 K in Fig. 16 corresponds to $\mu = 2090$ m^2/V s. Even higher mobilities have been reported by Shirahama and Kono[43] for lower holding fields.

However, below 0.5 K, the agreement between the experiments and the theoretical values given by Eq. (1) becomes less satisfactory. This is demonstrated in Fig. 8 at 0.6 K where the data lie slightly below the theoretical values. The
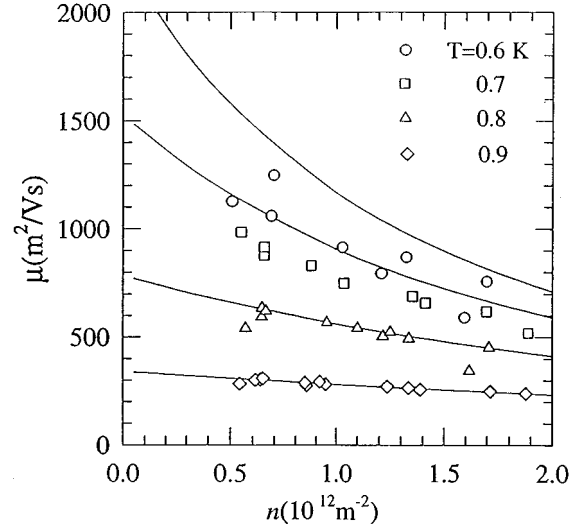
simplest interpretation of these results is that this increase in scattering rate is an indication of the quantization of the electron motion in the field of the other electrons (since $\hbar \omega_p / k \approx 0.3$ K for $n = 10^{12}$ m^{-2}). A similar phenomenon, though not so pronounced at the lower densities, is apparent in the results of Mehrotra *et al.*[19] This was interpreted by Mehrotra[46] as due to extra scattering from viscoelastic modes in the correlated electron fluid. In our experiments, the decrease in μ below 0.5 K is often accompanied by conductivity fluctuations which disappear at the transition to the solid phase. This may be related to the nonlinearity which becomes particularly strong once the system becomes a crystal.[43] Further details will be published elsewhere.

B. Magnetoconductivity: Vapor-atom scattering

For a classical or semiclassical system, deviations from the Drude model are expected for $B > B_0$, the onset field for magnetoresistivity. At 1 K, B_0 varies from 0.40 to 0.68 T as n increases from 0.5 to 2×10^{12} m^{-2}. This is particularly interesting above 1 K where the scattering from the gas atoms is quasielastic and short range and approximate to ideal δ-function scattering. The interaction is also essentially independent of the electron density and the vertical holding field. Hence this region is ideal for the comparison of experiment and theory. At 1.3 K, the scattering due to the ripplons can effectively be neglected. The overall field dependence of $1/\sigma$ at 1.3 K is shown in Fig. 9 for $n = 0.74$ and 2.32×10^{12} m^{-2} in fields from 0.1 to 8 T. Below 0.6 T a Drude-like region is observed, as discussed above, with $1/\sigma \propto B^2$, giving a mobility of 24 m^2/V s. The solid lines **d** and **d1** shows the fit to the Drude model. Above 0.8 T, $1/\sigma$ deviates from the line, though it continues to increase with field. The dashed line **s** shows the SCBA result, as given by van der Heijden *et al.*[25] for the highest density. Both the field dependence and the absolute magnitude of $1/\sigma$ are quite different, particularly in the field range from 0.3 to 6 T. The line **m** shows the many-electron theory, Eq. (9), valid for $B \gg B_0 = 0.70$ T here. However, at this temperature the contri-
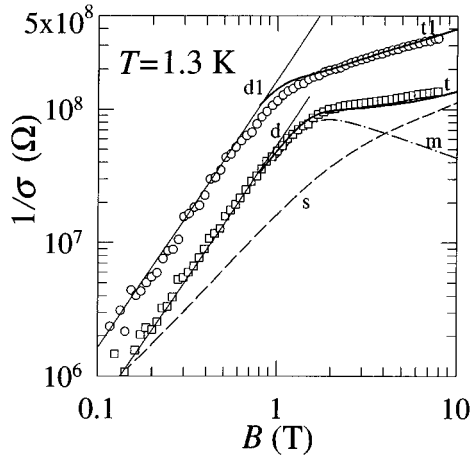
FIG. 9. The inverse conductivity $1/\sigma(B)$ vs B at 1.3 K for $n = 0.74$ ($\square$) and 2.32 ($\bigcirc$) $\times 10^{12}$ m^{-2}. The lines show the Drude model (lines **d** and **d1**), the independent electron model (line **s**) for the lowest density, the many-electron theory (line **m**) for the lowest density, and the total theoretical $1/\sigma$ (lines **t** and **t1**).

FIG. 10. (a) $\sigma(0)/\sigma(B)$ vs B^2 at 1.3 K for $n = 0.67$ ($\bigcirc$), 1.04 ($\triangledown$), 1.49 ($\square$), and 2.78 ($\diamondsuit$) $\times 10^{12}$ m^{-2}. The lines show the Drude model (line **d**), the independent electron theory (line **s**), and the quantum corrected Drude model (line **c**). (b) The full many-electron theory (lines **t1** to **t4**, decreasing density).

bution to the Landau level width from the collision broadening is quite significant, particularly above 3 T, and this is combined self-consistently with the many-electron result, using Eq. (11), to give the total $1/\sigma$ as shown in lines **t** and **t1**. This is in excellent agreement with the data at the higher fields. Figure 9 shows the general features of all the data. First there is a well pronounced Drude region, followed by a crossover to the many-electron theory above an onset field B_0. At the higher fields, the effects of collision broadening become more apparent and in the high field limit, dominate the magnetoconductivity, as in the SCBA theory.

A key prediction of the many-electron theory is that the onset field B_0 and the crossover from Drude to the many-electron or SCBA theories should be density dependent. This can be demonstrated by plotting the parameter $\sigma_0/\sigma(B)$ against B for a range of different electron densities, using the experimental values of $\sigma(B)$ and μ, as shown in Fig. 10. This plot normalizes each data set to the Drude-like B^2 dependence at low fields. The behavior which emerges from Fig. 10 is that $\sigma_0/\sigma(B)$ initially follows the universal Drude model (line **d**). A quantum corrected Drude model is also shown in which the scattering rate is field independent but the diffusion length changes from the classical cyclotron radius to the magnetic length. Above 1 T, $\sigma_0/\sigma(B)$ *saturates* and the saturated value increases with electron density, as given by Eq. (6). In the gas-atom scattering region the independent electron theory (SCBA) predicts that $\sigma_0/\sigma(B)$ should be independent of electron density, as discussed above, and is shown as the solid line **s** in Fig. 10 for a mean mobility of 24 m^2/vs. It can be seen that the data lie between the SCBA line and the Drude model and are density dependent. The SCBA represents the maximum possible scattering rate when the only limitation is the collision width of the Landau levels. The internal electric fields reduce the scattering rate and increase $1/\sigma$. Hence the measured $\sigma_0/\sigma(B)$ should follow the SCBA result only for very low densities (depending on the temperature and zero-field mobility) while for high densities the Drude model holds.
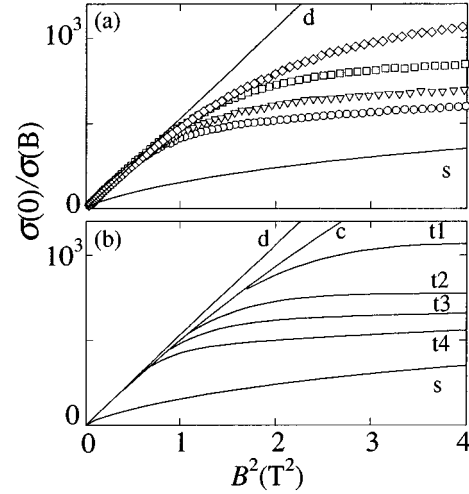
The low-field many-electron theory, Eq. (8), is plotted in Fig. 10(b) for the same densities as in Fig. 10(a). This demonstrates the deviations from the Drude model for $B > B_0$ and shows how this occurs at lower fields as the density is reduced. Above 3 T, the collision width of the Landau levels increases rapidly while the energy uncertainty due to the internal electric fields decreases, leading to a crossover to the SCBA result in higher fields as seen in Fig. 9. It should be stressed that there are no adjustable parameters in these calculations and hence these experiments constitute a strong confirmation of the theory.

Measurements of $1/\sigma(B)$ at 1.15 K are shown in Fig. 11 for $n = 0.46$ and 1.85×10^{12} m^{-2}. At low fields the Drude model (lines **d** and **d1**) is followed with a mobility $\mu = 42^{\pm}2$ m^2/V s. The dashed line **s** shows the single-particle
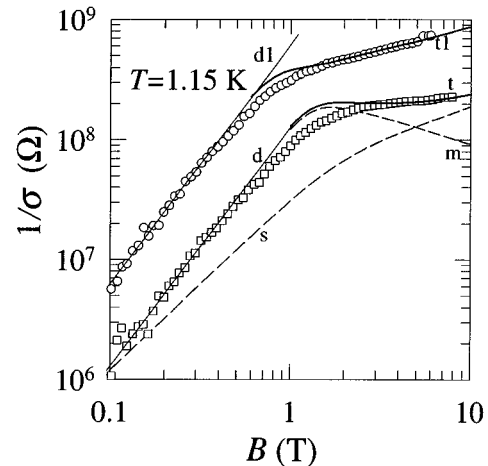

FIG. 11. The inverse conductivity $1/\sigma(B)$ vs B at 1.15 K for $n = 0.46$ ($\square$) and 1.85 ($\bigcirc$) $\times 10^{12}$ m^{-2}. The lines show the Drude model (lines **d** and **d1**), the independent electron model (line **s**) for the lowest density, the many-electron theory (line **m**) for the lowest density, and the total theoretical $1/\sigma$ (lines **t** and **t1**).
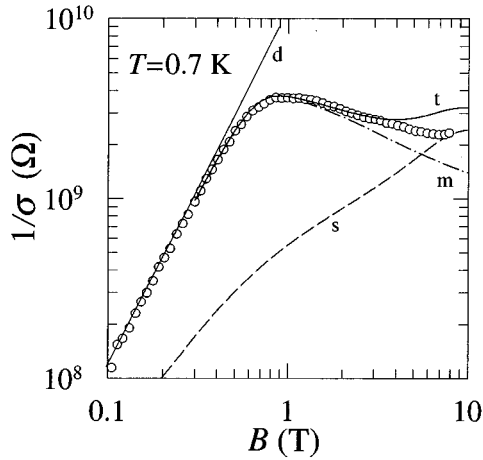
FIG. 12. The inverse conductivity $1/\sigma(B)$ vs B at 0.7 K for $n = 0.55 \times 10^{12}$ m^{-2}. The lines show the Drude model (line **d**), the independent electron model (line **s**), the many-electron theory (line **m**), and the total theoretical $1/\sigma$ (line **t**).

theory for this mobility. The deviation between the data and this SCBA result is greater than at 1.3 K, particularly near 1 T, though the data approaches the SCBA result at the highest fields, as before. The lines **t** and **t1** show the many-electron theory, including a significant contribution to the scattering from the ripplons at this temperature.

C. Magnetoconductivity: Ripplon scattering

Below 1 K, scattering by ripplons becomes the dominant mechanism. Figure 12 shows $1/\sigma$ versus B at 0.7 K for $n = 0.55 \times 10^{12}$ m^{-2}. As at higher temperatures, the data follow the Drude model (line **d**) to about 0.4 T before saturating at about 1 T as predicted by Eq. (6). However, below 1 K, the quantum limit $\hbar\omega_c/kT = 1.344B/T > 1$ is soon reached, and the diffusion length becomes the magnetic length l, which leads to a decrease in $1/\sigma$ with increasing field, as given in Eq. (12). The independent electron theory (line **s**) now lies well below the data for $B < 5$ T. The quantum many-electron theory (line **m**) is close to the experimental result between 1 and 2 T, while at higher fields, $1/\sigma$ increases due to collision broadening and the calculated total $1/\sigma$ is plotted as line **t**.

The change in $1/\sigma(B)$ with temperature is shown in Fig. 13 at 0.9, 0.8, 0.7, 0.6, and 0.4 K for densities close to 0.55×10^{12} m^{-2}. In the Drude region the mobility μ increases as the temperature falls, though the range of fields for which $1/\sigma \propto B^2$ decreases. The lines **t1** to **t5** show the total many-electron theory including ripplon and gas-atom scattering and the contribution for the collision broadening. As the field increases, the inverse conductivity saturates and even decreases slightly in the quantum limit, $\hbar\omega_c/kT > 1$. The overall agreement is excellent, with no adjustable parameters.

In order to demonstrate the saturation of $1/\sigma(B)$ with increasing field as the temperature falls, Fig. 14 shows $ne/\mu\sigma(B)$ vs B^2 for $n = 1.71 \times 10^{12}$ m^{-2} at 0.9, 0.8, 0.7, and 0.6 K, using the empirical Drude mobilities of 250, 430, 620, and 760 ± 20 m^2/V s. This particular plot normalizes each data set to the Drude-like B^2 dependence at low fields and
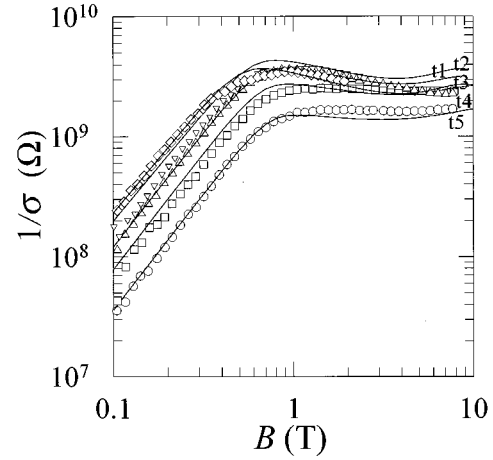

FIG. 13. The inverse conductivity $1/\sigma(B)$ vs B at 0.9 ($\bigcirc$), 0.8 ($\square$), 0.7 ($\triangle$), 0.6 ($\triangledown$), and 0.4 ($\diamondsuit$) K for $n = 0.54$, 0.57, 0.55, 0.51, and 0.60×10^{12} m^{-2} (the mobilities are 284, 540, 980, 1130, and 2090 m^2/V s, respectively). The lines show the full many-electron theory (lines **t1** to **t5**, increasing temperature).

hence is independent of random or systematic errors in the conversion from phase shift to conductivity. In each case the overall behavior is the same as already demonstrated in Fig. 13. The Drude model is initially followed (line **d**), due to many-electron effects. The parameter $ne/\mu\sigma$ then saturates above the onset field B_0. The saturation value, $\propto B_0^2$, decreases with decreasing temperature, as predicted by Eq. (6). The lines **t1** to **t4** show the many-electron calculations.

The density dependence of $1/\sigma$ at fixed temperature is shown in Fig. 15 at 0.9 K for $n = 0.54$, 0.85, 1.39, and 1.88×10^{12} m^{-2}. The mobility due to ripplon scattering is density-dependent through the effect of the vertical electric pressing field $E_\perp$ on the electron-ripplon interaction. The lines **t1** to **t4** again show the many-electron calculations, with good agreement.
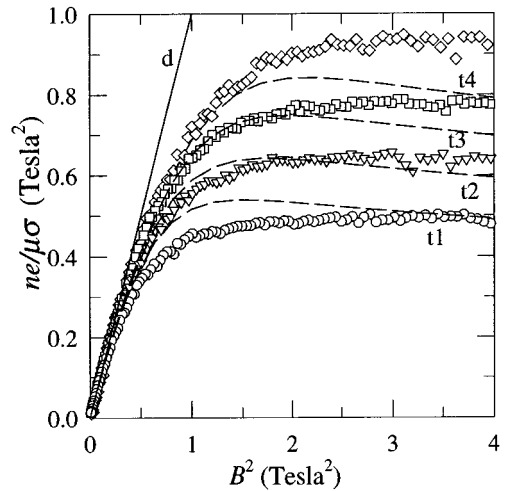

FIG. 14. The measured $ne/\mu\sigma(B)$ vs B^2 at 0.9 ($\diamondsuit$), 0.8 ($\square$), 0.7 ($\triangledown$), and 0.6 ($\bigcirc$) K for $n = 1.71 \times 10^{12}$ m^{-2} (the mobilities are 250, 430, 620, and 760 m^2/V s, respectively). The lines show the Drude model (line **d**) and the full many-electron theory (lines **t1** and **t4**, increasing temperature).
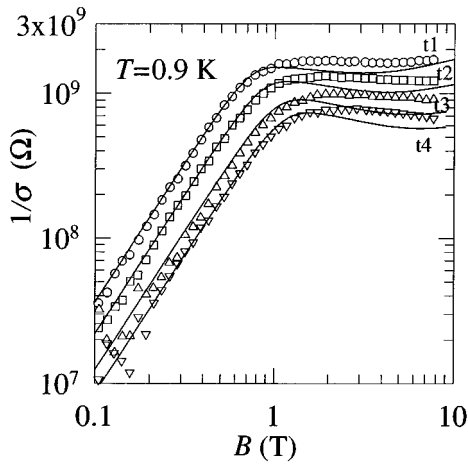
FIG. 15. The inverse conductivity $1/\sigma(B)$ vs B at 0.9 K for n = 0.54 (○), 0.85 (□), 1.39 (△), and 1.88 (▽) $\times 10^{12}$ m^{-2} (the mobilities are 284, 276, 257, and 238 m^2/V s, respectively). The lines show the full many-electron theory (lines **t1** to **t4**, increasing density).

To separate the density dependence due to the many-electron effects from the density dependence of the electron-ripplon interaction, we again plot $ne/\mu\sigma$ vs B as shown in Fig. 16 at 0.8 K for a range of electron densities, in magnetic fields up to 8 T. The parameter $ne/\mu\sigma$ follows the Drude model, saturates above the onset field B_0 and finally decreases at higher fields. The parameter $ne/\mu\sigma$ increases with electron density, as given by Eq. (9b). The independent electron, or SCBA, theory[28] for ripplons is shown (line **s**) for the lowest density. At this temperature where the mobility is very large, the SCBA overestimates $\sigma(B)$ by at least an order of magnitude at 1 T. The quantum many-electron theory, Eq. (12) is plotted (lines **t1**–**t4**, increasing density), including the contribution from the Landau level collision width (small
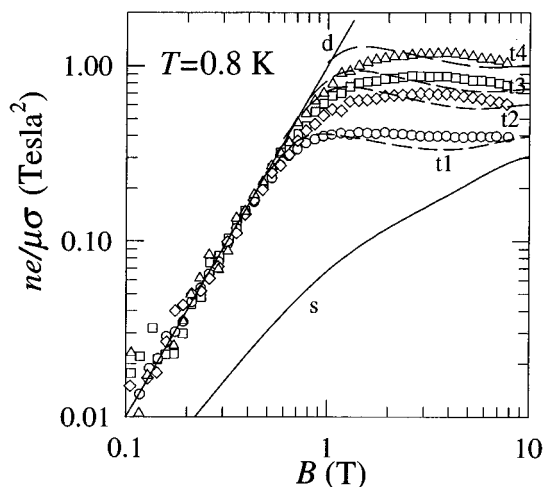

FIG. 16. The measured $ne/\mu\sigma(B)$ vs B at 0.8 K for n = 0.57 (○), 1.21 (◇), 1.62 (□), and 2.03 (△) $\times 10^{12}$ m^{-2} (the mobilities are 540, 403, 343, and 259 m^2/V s, respectively). The lines show the Drude model (line **d**) and the full many-electron theory (lines **t1** to **t4**, increasing density). The independent electron theory (line **d**) is shown for the lowest density.
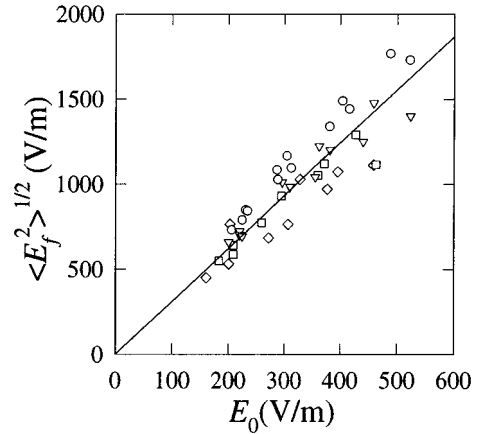

FIG. 17. Experimental values of the internal electric field E_f vs the scaling field E_0. The line shows $E_f = 3.1 E_0$.

below 3 T). As the field increases above 0.5 T, the experiments crossover from the Drude model to the many-electron theory, which holds for $\hbar\omega_c/kT > 2$. However, at higher fields, above 5 T, the collision time decreases and the data start to approach the independent-electron or SCBA result.

Conversely, we can use the measured $1/\sigma(B)$ at 2 T, to obtain experimental values of E_f. At this magnetic field $1/\sigma(B)$ lies clearly between the SCBA and Drude regions, and is proportional to B_0^2 and hence the internal electric field E_f. Each measurement of σ at 2 T can be used to derive a value of E_f. Figure 17 shows a plot of the experimental internal field E_f vs $E_0 = (n^{3/2}k_BT/4\pi\bar\varepsilon\varepsilon_0)^{1/2}$, as defined in Eq. (5). The points come from over 40 combinations of density and temperature between 0.6 and 0.9 K, where a comprehensive set of experiments were performed. Within the error bars the measured field is indeed proportional to E_0 with a constant of proportionality = 3.1 ± 0.1. This can be compared with $\sqrt{F} = 3.07 \pm 0.03$ from the Monte Carlo calculations where the uncertainty represents the variation for the range of Γ from 20 to 70 covered by these experiments. This good agreement confirms the interpretation of the magnetoconductivity in terms of the internal electric fields and the magnitude of **E**$_f$ from the Monte Carlo simulations.

V. CONCLUSIONS

In conclusion, we have measured the magnetoconductivity $\sigma(B)$ of the nondegenerate two-dimensional electron fluid on superfluid helium in both the gas-atom and ripplon scattering regimes. In low fields the Drude model is valid, due to the smearing of the quantised Landau levels by the internal fluctuating electric fields. Hence the zero-field mobility can be obtained and is in good agreement with theoretical calculations for $T > 0.5$ K. In the ripplon regime, the theory explicitly assumes that the electron-electron correlation time is less than the relaxation time for the loss of momentum to the ripplons.

At higher fields, $1/\sigma$ saturates and is then proportional to the fluctuating internal electric fields. The strong influence of these fields on the magnetoconductivity $\sigma(B)$ of electrons on liquid helium below 1 K has been demonstrated experimentally for $B < 8$ T for $0.25 < T < 1.3$ K. The magnitude and density dependence of $\sigma(B)$ cannot be explained using

independent-electron theories. The density and temperature dependence of the internal fields derived from the experiments are in excellent agreement with Monte Carlo simulations. These results explain the magnetotransport in a nondegenerate 2D electron fluid where the diffusion of the cyclotron orbits is dominated by Coulomb interactions.

APPENDIX

In the important case where the characteristic localization length in the direction normal to the surface is small compared to the thermal wavelength $\lambda_T = \hbar(2mkT)^{-1/2}$, the coefficients in Eq. (1) for the scattering rate τ_0^{-1} take on the form (cap units are used here to match Ref. 13).

$$E_1 \approx \frac{4\alpha_\perp^{(0)}kT}{e}(Y-1.018),$$

$$E_2^2 \approx 12\left(\frac{\alpha_\perp^{(0)}kT}{e}\right)^2 (1.949 - 2.703Y + Y^2), \qquad (A1)$$

$$Y = \frac{1}{2}\ln\left(\frac{2\hbar^2\alpha_\perp^2}{mkT}\right), \quad \alpha_\perp\lambda_T \ll 1. \qquad (A2)$$

The parameter $\alpha_\perp$ determines the decay of the electron wave function normal to the helium surface, and for a variational wave function of the form $\psi(z) \propto z\exp(-\alpha_\perp z)$ the equation for $\alpha_\perp$ is

$$\alpha_\perp = \alpha_\perp^{(0)}s, \quad s^3 - s^2 - \frac{3}{2}eE_\perp m\hbar^{-2}(\alpha_\perp^{(0)})^{-3} = 0,$$

$$\alpha_\perp^{(0)} = \frac{me^2}{4\hbar^2}\frac{\varepsilon-1}{\varepsilon+1}. \qquad (A3)$$

In the limit of "strong" classically strong magnetic fields where the magnetoconductivity as a function of B is close to saturation we have

$$\tau_B^{-1} = \frac{e^2E_\perp^2}{4\hbar\alpha_s}\left(\frac{B}{B_0}\right)^2\left[\pi^{-1/2}\ln\left(\frac{2B_T}{B}\right) + \frac{\widetilde{E}_1}{E_\perp} + \frac{\widetilde{E}_2^2}{E_\perp^2}\right], \qquad (A4)$$

$$B_T \gg B \gg B_0, \quad B_T = mkT/\hbar e \quad (B/B_T \equiv \hbar\omega_c/kT),$$

where

$$\widetilde{E}_1 \approx \frac{4\alpha_\perp^{(0)}kT}{\pi e}(Y-0.711),$$

$$\widetilde{E}_2^2 \approx 8\frac{(\alpha_\perp^{(0)})^2(kT)^2}{\pi e^2}(Y^2 - 2.423Y + 1.206). \qquad (A5)$$

In Eq. (A4) we have defined the characteristic field for the onset of magnetoresistance B_0 as

$$B_0 = \left(\frac{2\pi m^3 kT}{\hbar^2 e^2 \langle E_f^{-1}\rangle^2}\right)^{1/4}. \qquad (A6)$$

We note that the first term in the square brackets in Eq. (A4) is slightly smaller than the value which follows from the theory where the corrections $\approx \hbar\omega_c/kT$ are taken into account,[10] except in the range of extremely large $\hbar\omega_c/kT$ where these corrections become small. The dependence of this term on B is very smooth for $(mkT\hbar e) > B \gtrsim 2B_0$; it has been found numerically in Ref. 10. On the whole, the conductivity as given by Eqs. (6) and (A4) is nearly independent of B.

In the ultraquantum limit we have

$$\tau_B^{-1} = \frac{e^2E_\perp^2}{2\hbar\alpha_s}\frac{B_T^{3/2}B^{1/2}}{B_0^2}\left[1 + \frac{\hat{E}_1}{E_\perp}\frac{B}{B_T} + \frac{\hat{E}_2^2}{E_\perp^2}\frac{B^2}{B_T^2}\right], \quad B \gg B_T, \qquad (A7)$$

where

$$\hat{E}_1 \approx \frac{\alpha_\perp^{(0)}kT}{e}(\hat{Y}-1.018),$$

$$\hat{E}_2^2 \approx \frac{3(\alpha_\perp^{(0)})^2(kT)^2}{4e^2}(\hat{Y}^2 - 2.703\hat{Y} + 1.949),$$

$$\hat{Y} = \frac{1}{2}\ln\left(\frac{8\hbar\alpha_\perp^2}{eB}\right) \qquad (A8)$$

[in deriving (A8) we assumed that the magnetic length $l = (\hbar/eB)^{1/2} \gg \alpha_\perp^{-1}$]. For $B \gg B_T$ the magnetoconductivity $\sigma = (\hbar e^2 n/2mkT\omega_c)\tau_B^{-1}$, and it follows from (A7) that it increases with B. Expressions for the magnetoconductivity in the crossover region from the Drude behavior to the saturation and high field regions are given in Ref. 10.

---

[1] *2D Electron Systems on Helium and Other Substrates*, edited by E. Y. Andrei (Kluwer Academic, New York, 1997). For an introductory review, see W. F. Vinen and A. J. Dahm, Phys. Today **40**, 43 (1987).

[2] C. C. Grimes and G. Adams, Phys. Rev. Lett. **42**, 795 (1979); D. S. Fisher, B. I. Halperin, and P. M. Platzman, *ibid.* **42**, 798

(1979); E. Y. Andrei, F. I. B. Williams, D. C. Glattli, and G. Deville, in *The Physics of Low-dimensional Semiconductor Structures*, edited by P. Butcher *et al.* (Plenum, New York, 1993), Chap. 14, p. 499.

[3] J. Frost, P. Fozooni, M. J. Lea, and M. I. Dykman, Europhys. Lett. **16**, 575 (1991); M. I. Dykman, M. J. Lea, P. Fozooni, and

J. Frost, Phys. Rev. Lett. **70**, 3975 (1993); M. I. Dykman, M. J. Lea, P. Fozooni, and J. Frost, Physica B **197**, 340 (1994).

[4] M. J. Lea, P. Fozooni, P. J. Richardson, and A. Blackburn, Phys. Rev. Lett. **73**, 1142 (1994).

[5] A. Blackburn, K. Djerfi, M. I. Dykman, C. Fang-Yen, P. Fozooni, A. Kristensen, M. J. Lea, P. J. Richardson, A. Santrich-Badal, and R. W. van der Heijden, Czech. J. Phys. **46**, 3056 (1996), Suppl. 56.

[6] T. Ando and Y. Uemura, J. Phys. Soc. Jpn. **36**, 959 (1974); T. Ando, Y. Matsumoto, and Y. Uemura, *ibid*. **39**, 279 (1974); T. Ando, A. B. Fowler, and F. Stern, Rev. Mod. Phys. **54**, 437 (1982).

[7] M. I. Dykman, Phys. Status Solidi B **88**, 463 (1978).

[8] P. W. Adams and M. A. Paalanen, Phys. Rev. B **37**, 3805 (1988); **38**, 5064(E) (1988).

[9] Yu. Z. Kovdrya, V. A. Nikolayenko, O. I. Kirichek, S. S. Sokolov, and V. N. Grigor'ev, J. Low Temp. Phys. **91**, 371 (1993); J. Neuenschwander, W. Joss, and P. Wyder, Helv. Phys. Acta. **65**, 325 (1992); Physica B **194–196**, 1231 (1994).

[10] M. I. Dykman and L. S. Khazan, Zh. Eksp. Teor. Fiz. **77**, 1488 (1979) [Sov. Phys. JETP **50**, 747 (1979)].

[11] S. Edel'man, Sov. Phys. JETP **50**, 338 (1979); L. Wilen and R. Giannetta, Phys. Rev. Lett. **60**, 231 (1988).

[12] S. Ito, K. Shiraham, and K. Kono, Czech. J. Phys. **46**, Suppl. S1, 339 (1996).

[13] M. I. Dykman, C. Fang-Yen and M. J. Lea, Phys. Rev. B (to be published). (PPI-BQ5969)

[14] W. T. Sommer and D. J. Tanner, Phys. Rev. Lett. **27**, 1345 (1971).

[15] A. S. Rybalko, B. N. Esel'son, and Yu. Z. Kovdrya, Fiz. Nizk. Temp. **42**, 795 (1979).

[16] Y. Iye, J. Low Temp. Phys. **40**, 441 (1980).

[17] C. C. Grimes and P. W. Adams, Phys. Rev. Lett. **36**, 145 (1976).

[18] V. A. Buntar', Yu. Z. Kovdrya, V. N. Grigoriev, Yu. P. Monarhka, and S. S. Sokolov, Fiz. Nizk. Temp. **13**, 789 (1987) [Sov. J. Low Temp. Phys. **13**, 451 (1987)]; V. A. Buntar', V. N. Grigoriev, O. I. Kirichek, Yu. Z. Kovdrya, Yu. P. Monarhka, and S. S. Sokolov, J. Low Temp. Phys. **79**, 323 (1990); Yu. P. Monarkha and S. S. Sokolov, Fiz. Nizk. Temp. **5**, 1283 (1979); S. S. Sokolov, G-Q. Hai, and N. Studart, Phys. Rev. B **51**, 5977 (1995).

[19] R. Mehrotra, C. J. Guo, Y. Z. Ruan, D. B. Mast, and A. J. Dahm, Phys. Rev. B **29**, 5239 (1984).

[20] M. A. Stan and A. J. Dahm, Phys. Rev. B **40**, 8995 (1989).

[21] M. Saitoh, J. Phys. Soc. Jpn. **42**, 201 (1977).

[22] V. B. Shikin, Zh. Eksp. Teor. Fiz. **60**, 713 (1971) [Sov. Phys. JETP **33**, 387 (1971)]; V. B. Shikin and Yu. P. Monarkha, J. Low Temp. Phys. **16**, 193 (1974); P. M. Platzman and G. Beni, Phys. Rev. Lett. **36**, 626 (1976).

[23] M. J. Lea and M. I. Dykman, Philos. Mag. B **69**, 1059 (1994).

[24] R. Kubo, S. J. Miyake, and N. Hashitsume, Solid State Phys. **17**, 269 (1965).

[25] R. W. van der Heijden, M. C. M. van de Sanden, J. H. G. Sure-waard, A. Th. A. M. de Waele, H. M. Gijsman, and F. M. Peeters, Europhys. Lett. **6**, 75 (1988).

[26] J. Neuenschwander, P. Scheuzger, W. Joss, and P. Wyder, Physica B **165&166**, 845 (1990); P. Scheuzger, J. Neuenschwander, and P. Wyder, Helv. Phys. Acta **64**, 170 (1991); P. Scheuzger, J. Neuenschwander, W. Joss, and P. Wyder, *ibid*. **65**, 325 (1992); Physica B **194–196**, 1231 (1994).

[27] P. J. M. Peters, P. Scheuzger, M. J. Lea, Yu. P. Monarkha, P. K. H. Sommerfeld, and R. W. van der Heijden, Phys. Rev. B **50**, 11 570 (1994).

[28] M. Saitoh, Solid State Commun. **52**, 63 (1984).

[29] M. I. Dykman, J. Phys. C **15**, 7397 (1982).

[30] C. Fang-Yen, M. I. Dykman, and M. J. Lea, Phys. Rev. B (to be published). (PPII-BT5892)

[31] R. C. Gann, S. Chakravarti, and G. V. Chester, Phys. Rev. B **20**, 326 (1979); J. P. Hansen, D. Levesque, and J. J. Weiss, Phys. Rev. Lett. **43**, 979 (1979).

[32] L. D. Landau and E. M. Lifshitz, *Theoretical Physics, Vol. 2: Quantum Mechanics* (Pergamon, Oxford, 1977).

[33] Supplied by Professor P. V. E. McClintock, Dept. of Physics, University of Lancaster, U.K. The ^{3}He/^{4}He atomic ratio was less than 10^{-13}.

[34] B. N. Eselson, A. S. Rybalko, and S. S. Sokolov, Fiz. Nizk. Temp. **6**, 611 (1980) [Sov. J. Low Temp. Phys. **6**, 544 (1980)].

[35] A. Blackburn *et al.* (unpublished).

[36] R. Mehrotra and A. J. Dahm, J. Low Temp. Phys. **67**, 541 (1987); L. Wilen and R. Giannetta, *ibid*. **72**, 353 (1988); A. Thom and C. J. Apelt, *Field Computations in Engineering and Physics* (van Nostrand, London, 1961).

[37] M. Ilino, M. Suzuki, and A. J. Ikushima, J. Low Temp. Phys. **61**, 155 (1985).

[38] J. Neuenschwander, P. Scheuzger, W. Joss, and P. Wyder, Physica B **165/166**, 845 (1990); J. Frost, M. J. Lea, and P. Fozooni, Cryogenics **31**, 890 (1991).

[39] S. Yücel, L. Menna, and E. Y. Andrei, Phys. Rev. B **47**, 12 672 (1993).

[40] P. J. M. Peters, M. J. Lea, A. M. L. Janssen, A. O. Stone, W. P. N. M. Jacobs, P. Fozooni, and R. W. van der Heijden, Phys. Rev. Lett. **67**, 2199 (1991).

[41] P. K. H. Sommerfeld (private communication); K. Kono, U. Albrecht, and P. Leiderer, J. Low Temp. Phys. **82**, 279 (1991).

[42] M. J. Lea, A. O. Stone, P. Fozooni, and J. Frost, J. Low Temp. Phys. **85**, 67 (1991); M. J. Lea, P. Fozooni, and J. Frost, *ibid*. **92**, 189 (1993).

[43] K. Shirahama and K. Kono, Phys. Rev. Lett. **74**, 781 (1995); A. Kristensen, K. Djerfi, P. Fozooni, M. J. Lea, P. J. Richardson, A. Santrich-Badal, A. Blackburn, and R. W. van der Heijden, *ibid*. **76**, 1154 (1996); K. Kono and K. Shirahama, Surf. Sci. **361/362**, 826 (1996); K. Shirahama and K. Kono, J. Low Temp. Phys. **104**, 237 (1996).

[44] G. Deville, J. Low Temp. Phys. **72**, 135 (1988).

[45] K. Shirahama, S. Ito, H. Suto, and K. Kono, J. Low Temp. Phys. **101**, 4349 (1995).

[46] R. Mehrotra, J. Low Temp. Phys. **79**, 311 (1990).